FORM 71-12
8/94

WAPD-T-3130

CONF-970832--

The Relationship Between Observed Stress Corrosion Cracking Fracture Morphology and Microstructure in Alloy 600

D. M. Symons and M. G. Burke
Westinghouse Electric Corporation
Bettis Atomic Power Laboratory
West Mifflin, PA 15122

J. P. Foster
Westinghouse Electric Corporation
Westinghouse Science and Technology Center
Pittsburgh, PA 15235

DE-AC11-93PN38195

BETTIS ATOMIC POWER LABORATORY WEST MIFFLIN, PENNSYLVANIA 15122-0079

Operated for the U.S. Department of Energy
by WESTINGHOUSE ELECTRIC CORPORATION

DISCLAIMER

The Relationship Between Observed Stress Corrosion Cracking Fracture Morphology and Microstructure in Alloy 600

D. M. Symons
Westinghouse Electric Corp
Bettis Atomic Power Laboratory
West Mifflin, PA 15122
(412) 476-7379

J. P. Foster
Westinghouse Electric Corp
Westinghouse STC
Pittsburgh, PA 15235
(412) 256-1060

M. G. Burke
Westinghouse Electric Corp
Bettis Atomic Power Laboratory
West Mifflin, PA 15122
(412) 476-5883

Abstract

Microstructure is known to influence the stress corrosion cracking (SCC) behavior of Alloy 600 in both hydrogenated water and steam environments. This study evaluated the relative SCC response of a single heat of Alloy 600 as a function of microstructure in a hydrogenated doped-steam environment. The 400°C doped-steam environment was selected for the SCC tests to accelerate cracking. The material was evaluated in three conditions: 1) as-received 2) as-annealed and 3) as-annealed + 26% deformation. Microstructural characterization was performed using analytical electron microscopy (AEM) techniques for the evaluation of carbide type and morphology, and general structure. Constant displacement (bolt-loaded) compact tension specimens were used to induce SCC. The as-annealed and as-annealed plus cold worked samples had two fracture morphologies: a rough intergranular SCC fracture morphology and a smooth intergranular fracture morphology. The SCC fracture in the as-received specimens was characterized by a classic intergranular morphology at low magnification, consistent with the microstructural evaluation of cross-sectional metallographic samples. More detailed examination revealed a "pseudo-intergranular" fracture morphology. This "psuedo-intergranular" morphology appears to be comprised of very fine cleavage-like microfacets. These observations may assist in understanding the difference in SCC fracture morphologies as reported in the open literature.

I. Introduction

Stress corrosion cracking (SCC) of Alloy 600 has been observed in pressurized water reactors components (References 1-2). Previous studies have shown that the SCC behavior is dependent on the microstructure, most notably on the precipitation of Cr-rich carbides (primarily M_7C_3) along the grain boundaries (References 2-4), and the degree of cold work (Reference 5). The formation of a "continuous" intergranular carbide network enhances the resistance to SCC whereas "clean" or carbide-free grain boundaries are susceptible to intergranular (IG) SCC in pressurized water environments. Materials with extensive intergranular carbide precipitation exhibit enhanced resistance to pressurized water (PW) SCC, even though pronounced Cr depletion can be associated with these intergranular carbides (Reference 6). Recently, creep behavior has been shown to be important in understanding the SCC behavior of these alloys (Reference 7). The degree of carbide precipitation may be important in controlling the deformation behavior (Reference 8). To develop a preliminary understanding of the role of microstructure on the SCC behavior, Alloy 600 specimens of a single heat were tested with various microstructures.

To accelerate cracking, a 400°C doped steam environment was selected for the SCC tests. This technique has been shown to be effective in prior work (Reference 9). The purpose of this study is to evaluate the relative SCC response of a single heat of Alloy 600 in a doped steam test environment as a function of material microstructure (precipitation and cold work). The fracture morphology was related to the fine scale microstructure and the crack growth rates were related to yield strength. These observations may assist in understanding the difference in SCC fracture morphologies as reported in the open literature (References 5,10).

II. Experimental Techniques

Material

The specimens for this program were obtained from a single plate of Alloy 600. The material was received in the hot worked and annealed condition, 982°C for 1 h followed by an air cool. The chemical composition of this alloy is listed in Table 1.

TABLE 1. Composition of Alloy 600 (wt.%)

Ni	Cr	Fe	Ti	Mn	Si	C	S	P	B
75	15	7.7	0.34	0.25	0.23	0.07	0.001	0.003	0.008

The original plate was sectioned into three pieces. Two of the pieces were heat treated at 1075°C for 24 h followed by a furnace cool. After heat treatment, the as-received plate and one of the heat treated plates were machined into large tensile bars with a 38 cm gage length, 7.5 cm width and 5 cm thickness. The axis of the tensile bar was parallel to the rolling direction. The as-received tensile bar was uniaxially strained 5% and the heat treated tensile bar was

uniaxially strained 26% to give the three material conditions that were subsequently tested as compact tension specimens. The ambient temperature tensile properties of the alloys in these three conditions are presented in Table 2.

TABLE 2: Ambient Temperature Tensile Properties

Heat Treat	Yield Stress (MPa)	True Stress at Max Load(MPa)	El. to Failure	Unif. El.
As-received +5%CW **AR+5**	460	940	43%	33%
1075°C/ 24 h/ FC **HT**	185	910	51%	42%
1075°C/ 24 h/ FC/ 26%CW **HT+CW**	770	920	23%	11%

Microstructural Characterization: LOM/AEM

The microstructure of these materials was examined using light optical metallography (LOM) and analytical electron microscopy (AEM). The metallographic specimens for LOM were etched in 2% Br-CH_3OH solution.

Thin-foil AEM specimens were prepared using a conventional twin-jet polisher with an electrolyte of 20% $HClO_4$ - 80% CH_3OH at approximately -40°C. The thin-foil samples were subsequently examined in Philips CM30, CM12, and EM420T analytical electron microscopes. Cr concentration profiles were measured for selected materials in the scanning transmission electron microscope (STEM) mode using energy dispersive x-ray spectroscopy (EDS) techniques in the Philips CM12 AEM equipped with an Oxford Instruments windowless light element EDS spectrometer. The nominal probe size for the analyses was 5 nm.

Doped Steam SCC Tests

Compact tension specimens were machined out of each plate from the same orientation. The CT specimens machined from the AR+5 and the HT conditions had a thickness of 20.3 mm and a width of 40.6 mm. The compact tension specimens machined from the HT+CW condition had a thickness of 17.8 mm and a width of 35.6 mm. Relative to the uniaxial straining direction, the specimens were in the L-T orientation. All specimens were precracked with a final K_{max} of 17 MPa√m and an average normalized crack length (a/W) of 0.4-0.5. The initial applied stress intensity factors for the specimens are shown in Table 3.

TABLE 3: Test Matrix for Specimens in Doped Steam

Specimen ID	Heat treatment	Applied Stress Intensity Factor MPa√m	Loading Method
S600-18	AR+5	48	Bolt-loaded
S600-22	AR+5	36	Bolt-loaded
S600-23	AR+5	24	Bolt-loaded
CB20-74	HT	36	Bolt-loaded
15-16	HT	36	Wedge-loaded
S34-56	HT+CW	33	Bolt-loaded

Most specimens (all except 15-16) were bolt loaded using a load transfer technique. The specimens were loaded to 95% of the final load in a tensile machine, then the load was transferred to the specimen while maintaining the crack mouth opening displacement (CMOD) constant as measured by a clip gage. This method works well for the higher strength materials, i.e., the as-received and the heat-treated + cold-worked specimens. Less than 5% load loss was observed for these specimens. The bolt-loaded heat-treated specimen with the low yield strength showed extensive load relaxation, ~30%. Therefore, specimen 15-16 was wedge loaded prior to test. This was performed by pressing a wedge between the notch flanks. The thickness of the wedge was determined by analyzing the trace of the front face displacement versus the load for an identical specimen. The wedge-loaded specimen showed little load relaxation. While the relaxation cannot be directly measured in the wedge-loaded specimen, it may be approximated from the calculated initial load and the measured final load. This produced a relaxation of between 0 and 3%. Therefore, a comparison of SCC behavior can be made between the wedge-loaded HT specimen and the bolt-loaded AR and HT+CW specimens.

The specimens were loaded into an autoclave that contained doped water, but were located above the water line. The required water chemistry was obtained by adding 100 ppm of each of the following sodium salts: chloride, fluoride, sulfate and nitrate. The autoclave was sealed and heated to 400°C at a pressure of 20.7 MPa that included a

hydrogen partial pressure of 76 KPa to produce a stagnant, superheated steam environment. The specimens were exposed to the doped steam environment for intervals of 60 to 100 h. After each interval, the surface crack length was measured on each specimen using an optical measurement technique. The change in stress intensity factor as the crack grew was calculated assuming no load relaxation with the compliance equations of Saxena and Hudak (reference 11). The assumption of no load relaxation was evaluated on some specimens by measuring the residual load on the specimens at the end of the test.

Post-test evaluation

After the test, selected specimens were sectioned in half, so as to preserve a complete cross-section of the precrack and stress corrosion crack for subsequent metallographic analysis. One of the cross-section samples was then mechanically fatigued to failure so that the stress corrosion fracture surface could be characterized using scanning electron microscopy (SEM). The remaining half of the sample was mounted and polished for metallographic evaluation. The metallographic specimens were etched in a 2% Br-CH_3OH prior to optical metallographic or SEM examination.

III. Results

Microstructural Characterization

The as-received microstructure with 5% cold work had a duplex grain structure with the grain size varying form 15 to 150 μm in size, Figure 1. Further, this specimen exhibited carbide "banded" regions. AEM showed both intergranular and intragranular M_7C_3 carbides that ranged from 0.5 to 4μm; more intragranular carbides were observed in the fine grained regions, Figure 2. Further AEM examination showed a pronounced dislocation substructure consisting of fine (~0.5 to 1μm), well-defined, clean subgrains throughout the material, Figure 3.

An increase in grain size was noted after the 24 h anneal at 1075°C. The grains ranged from ~ 20 to 350 μm in size, Figure 4, in a banded structure consisting of fine grained regions and coarse grained regions. The dislocation sub-grain structure was completely eliminated, as evidenced from the AEM analysis. This solution-annealing treatment did not, however, eliminate the "ghost" boundaries in this material. The ghost boundaries are M_7C_3 carbides that did not dissolve during the solution treatment while the grain boundaries moved away from the carbides. Residual dislocations were observed throughout the sample, Figure 5. The experimental STEM-EDS data for this material confirmed that the minimum Cr concentration in the vicinity of the grain boundary was ~ 11 wt.%. Cr depletion was observed up to 150 nm from the grain boundary as shown in Figure 6. This depletion of Cr was only noted for the M_7C_3 carbides that formed upon cooling from the solution-annealing temperature. No depletion was observed in the vicinity of the coarse, globular M_7C_3 carbides.

The addition of 26% cold work resulted in a highly deformed dislocation structure consisting of many slip bands, as shown in Figure 7a. The intersection of the slip bands with grain boundary carbides resulted in cracked grain boundary carbides, Figure 7b. These sights may act as crack nuclei.

SCC Data

The crack extension data are plotted in Figure 8 and the growth rates are plotted in Figure 9. The test data show that the AR+CW material is more susceptible to stress corrosion cracking than the HT material, with measurable crack growth in the first 100-h exposure. The crack growth rates of the HT material is also consistently below that for the AR condition. The crack extension measured for the HT+CW specimen was greatest in the first 100-h exposure (2.87 mm), but then the crack growth rate decreased by ~ 50%. This was within the scatter of the experimental data. The crack incubation times were calculated by back extrapolating the crack extension to 0. The crack incubation times were lower for the HT+CW specimen than for the AR+CW condition while the crack growth rates were similar. The HT material exhibited the most resistance to crack incubation as well as crack growth. The SCC in this environment shows a large range of Stage II (independent of applied stress intensity factor) crack growth rate behavior. It appears that for the as-received material at a K_I of 14-16 MPa$\sqrt{m}$, the crack growth shows a decreasing trend, suggesting the onset of Stage I crack growth and approaching a mechanically based threshold. The growth rates observed in the doped steam environment are similar to the rates observed in hydrogenated water environments (Reference 5) suggesting that the role of doped steam is to dramatically reduce the incubation time.

Metallographic & Fractographic Observations

As-received + 5%CW (AR - Sample S600-18)

Metallographic examination of this sample revealed extensive intergranular cracking, Figures 10 and 11, and a high proportion of secondary intergranular cracks. No evidence of transgranular cracking was obtained by optical metallography. The SEM observations were similar to those obtained by LOM. Figure 11 contains various examples of the intergranular cracks. Only one small

region, Figure 11b, showed what might be a "transgranular crack," although the "crack" is less than 5 μm from the grain boundary.

Low magnification SEM (100X) examination of this specimen revealed a classic smooth intergranular fracture surface, as shown in Figure 12. However, more detailed evaluation showed that the fracture surface was not smooth intergranular, but a "pseudo-intergranular" fracture. The "pseudo-intergranular" fracture is comprised of extremely fine crystallographic facets near the grain boundary. The fracture is proposed to follow the crystallographic nature but remain near the boundary due to the enhanced local hydrogen concentration. Figure 13 shows the "pseudo-intergranular" fracture morphology observed in this material after the doped steam test. This was described in more detail in Reference 12.

24h/1075°C/FC + 26%CW (HT+CW - Sample S34-56)

The SEM micrographs obtained from the polished and etched cross-section sample clearly showed the intergranular nature of the primary and secondary cracks, Figure 14. In addition to the intergranular cracks, the presence of "ghost" boundaries and real grain boundaries can be observed in Figure 14 because the Br-methanol solution can reveal different grain orientations due to crystallographic etching effects. Thus, the crack path evident in Figure 14 is truly intergranular. Figure 15 shows a carbide-decorated grain face that lies parallel to the surface of the sample. The dendritic nature of the "semi-continuous" intergranular M_7C_3 carbides is clearly visible. The observation of the grain face is identical to the fracto-graphic features further showing that the features on the SCC surface are impressions of grain boundary carbides.

Low magnification SEM examination of the fracture surface of this material revealed an intergranular SCC morphology, Figure 16. The banded grain structure (coarse/fine/coarse) in this material is clearly evident in the intergranular fracture surface shown in Figure 16. More detailed SEM study of this fracture surface showed that it was actually a complex fracture containing some areas of smooth intergranular and rough intergranular fracture. Figure 17 contains several examples of the smooth intergranular fracture morphology, with numerous discrete globular carbides embedded in the fracture surface. The micrographs of Figure 18 present a distinctly different fracture morphology that is the rough intergranular fracture morphology. Further examination of these fractures surfaces showed that the rough intergranular regions were, in fact, related to the complex intergranular carbide morphologies, particularly the dendritic M_7C_3. The dendritic carbide morphology is evident in the higher magnification micrographs of Figure 18. It is proposed that the rough intergranular surface corresponds to the outline of the grain boundary carbides. Figure 19 shows a "mixed" region containing some smooth intergranular fracture with coarse carbides and regions with the dendritic intergranular carbides.

24h/1075°C/FC (HT - Sample 15-16)

SEM examination of the metallographic cross-section of the sample revealed numerous branched intergranular cracks in addition to the primary intergranular crack. Examples are shown in Figure 20. No evidence of transgranular fracture was observed. The intergranular morphology of the SCC fracture is evident in Figure 21. Higher magnification examination, Figure 22, of this specimen revealed both smooth intergranular regions and some rough intergranular areas. The smooth intergranular regions were associated with the coarse discrete carbides; stereo images confirmed that some coarse carbides were "pulled" out of the grains. Some dendritic-type intergranular carbides were also observed on the fracture surface, but the evaluation was complicated by the presence of surface oxide. These were similar to the features shown in Figure 19. The sample appeared very similar to the HT+CW specimen, though with much less crack extension. Comparing HT and HT+CW, the cold work did not appear to affect the fracture morphology, only the growth rate.

IV. Discussion

The results of the doped steam test provided a ranking of the *relative* SCC susceptibility of the specimens as a function of material condition. As previously discussed, the heat treated material showed the most resistance to SCC. The heat-treated + cold worked condition and the as-received condition may be compared to the heat-treated condition to obtain a better understanding of the role of microstructure in SCC. Comparing the HT and HT+CW, suggests that by increasing the yield strength of the material by cold working, the susceptibility to SCC was dramatically increased. The enhancement of cracking by cold-work observed in this study is consistent with other investigations of SCC in Alloy 600 in primary water environments. The cold work greatly increased the mechanical driving force for SCC while only having small effects on the chemical driving force, electrochemical potential. Part of the role of cold work may be to create defects (observed as cracked carbides) preexisting on the grain boundaries. When a crack intersects a preexisting defect, the crack is advanced by the length of the defect. More importantly, the defect may act as a local strain concentrator. While the testing was performed in the Stage II regime, which is conventionally considered to be dominated by environmental factors, this testing suggests that mechanical

aspects also play an important role in SCC in the Stage II crack growth rate regime.

A comparison of the AR condition and the HT condition show two important differences. The as-received condition has both a higher yield strength and a smaller percentage of the grain boundaries covered with carbides. Both of these factors have been shown to be important in SCC susceptibility. The higher yield strength, again, leads to a higher mechanical driving force for SCC. The decreased coverage of the grain boundaries by carbides has been shown in the literature to decrease the resistance to SCC (reference 2-4). These two factors may both be contributing causes to the decrease in SCC behavior of the as-received material as compared to the heat treated material. Furthermore, the subgrain structure may alter the deformation behavior, leading the localized deformation and the crystallographic fracture termed "pseudo-intergranular".

The AR materials tested in doped steam was characterized by the "pseudo-intergranular" fracture. The microstructural changes induced by the heat treatment (precipitation of intergranular dendritic-type M_7C_3 carbides, etc.) were reflected by pronounced changes in the apparent fractography of SCC. The regions of rough intergranular fracture observed in the HT+CW sample were, in fact, associated with the presence of the dendritic M_7C_3 carbides. Both the size and morphology of these features/carbides were consistent with the previous microstructural data obtained by AEM.

The surface crack extensions measured for the AR and HT+CW specimens showed good agreement with the extent of SCC as measured from the fracture surfaces. The least susceptible material condition, as-heat-treated, showed the greatest variance in extent of cracking between the sample surface and fracture surface measurements. Such variation in crack length during SCC "initiation" is expected. The SCC cracking incubates in the center of the specimen and grows both in the width and thickness directions. When the crack extends to the surface, the crack growth is mostly uniform in the width direction.

These results suggest that the fine scale microstructure is a key component in understanding the SCC behavior of Alloy 600. This further shows that incubation and growth are dependent on the microstructure. SCC testing in conjunction with careful fractographic characterization and material characterization are leading to a better understanding of SCC.

V. Conclusions

1. The doped steam SCC test results show that the heat treated material is the most resistant to SCC of the three conditions tested. Increasing the yield strength, through cold work, or altering the microstructure, low grain-boundary carbide coverage and moderate yield strength increases, decreased the SCC resistance.
2. The presence of dendritic-type M_7C_3 intergranular carbides and the elimination of the dislocation substructure in the as-heat-treated specimens are associated with a reduction in SCC susceptibility over the same alloy in the as-received condition in the doped steam test.
3. A rough intergranular SCC fracture morphology observed in the heat-treated + cold-worked specimens are related to the intergranular dendritic-type M_7C_3 carbides whereas the smooth intergranular fracture faces were associated with the coarse globular carbides.
4. Cold-work enhances SCC of Alloy 600 in the doped steam test, in agreement with other investigations of Alloy 600 SCC behavior in pressurized water reactor environments. One effect of the cold work is to create grain boundary voids due to localized deformation prior to insertion into the environment.

Acknowledgments

The authors thank Mr. B.F. Kammenzind for technical discussions and review. This work was supported by DOE contract DE-AC11-93PN38195.

References

1) H.Coroiu, et al. "High Temperature Stress Corrosion Cracking on Inconel in Water," **Third Metallurgical Symposium on Corrosion**, 1959, (North Holland Pub. Co., Amsterdam, 1960), pp. 161-169.
2) D. Van Rooyen, "Review of the Stress Corrosion Cracking of Inconel 600," **Corrosion 31**, 1975, pp. 327-337.
3) H. A. Domain, R. H. Emanuelson, L. Katz, L. W. Sarver, and G. J. Theus, "Effect of Microstructure on Stress Corrosion Cracking of Alloy 600 in High Purity Water," **Corrosion 33**, 1977, pp. 26-37.
4) G. P. Airey, "The Effect of Carbon Content and Thermal Treatment on the Stress Corrosion Cracking Behavior of Inconel Alloy 600 Steam Generator Tubing," Paper 195 presented at CORROSION /78,Houston, TX.
5) M. O. Speidel and R. Magdowski, "Stress Corrosion Cracking of Nickel-Base Alloys in High Temperature Water," in **Sixth International Symposium on Environmental Degradation on**

Materials in Nuclear Power Systems-Water Reactors, Eds. Gold and Simonen, 1993, pp. 361-371.

6) G. S. Was and V. B. Rajan, "The Mechanism of Intergranular Cracking of NiCrFe Alloys in Sodium Tetrathionate," **Met Trans. 18A**, 1987, pp. 1313-1323.

7) J. K. Sung and G. S. Was, "Intergranular Cracking of Ni-16Cr-9Fe Alloys in High Temperature Water," **Corrosion 47**, 1991, pp. 824-834.

8) S. M. Bruemmer, L. A. Charlot, and C. H. Henager, "Microstructure and Microdeformation Effects on IGSCC of Alloy 600 Steam Generator Tubing," **Corrosion 44**, 1988, pp. 782-788.

9) J. A. Begley, "Evaluation of the Leak and Burst Characteristics of Roll Transition Regions Containing Primary Water SCC Cracks," **Proceedings of PWSCC Remedial Measures Workshop, EPRI, NP-6719-SD**, April 1990.

10) R. Rios, T. Magnin, D. Noel and O. de Bouvier, "Critical Analysis of Alloy 600 SCC Mechanisms in Primary Water," **Met. Trans., 26A**, 1995, pp. 925-939

11) Saxena, A. and Hudak, S. J., **International Journal of Fracture, Vol. 14, No. 5**, 1978, pp. 453-468.

12) M. G. Burke and D. M. Symons, Microstructural Effects on the SCC Morphology in Deaerated Water, **4th EPRI Workshop on PWSCC of Alloy 600**, Daytona Beach, Fl, Feb. 25-27, 1997

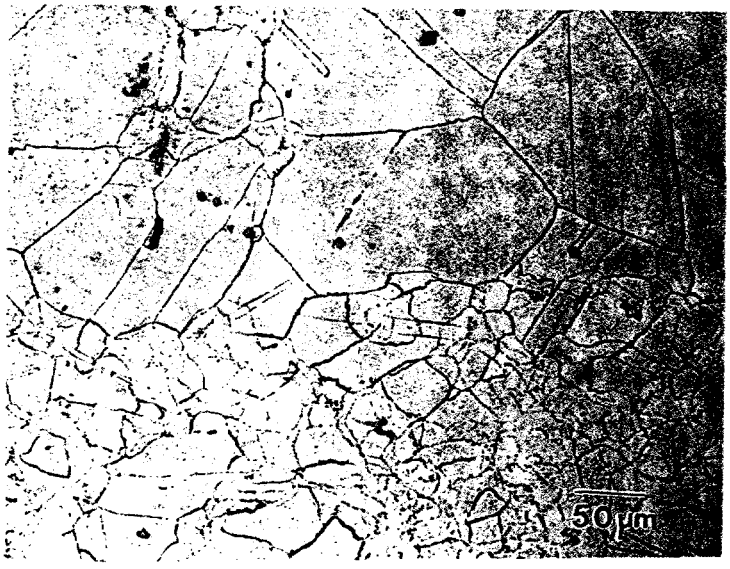

Figure 1: Light Optical Micrograph of the As-Received Material Showing Duplex Grain Structure

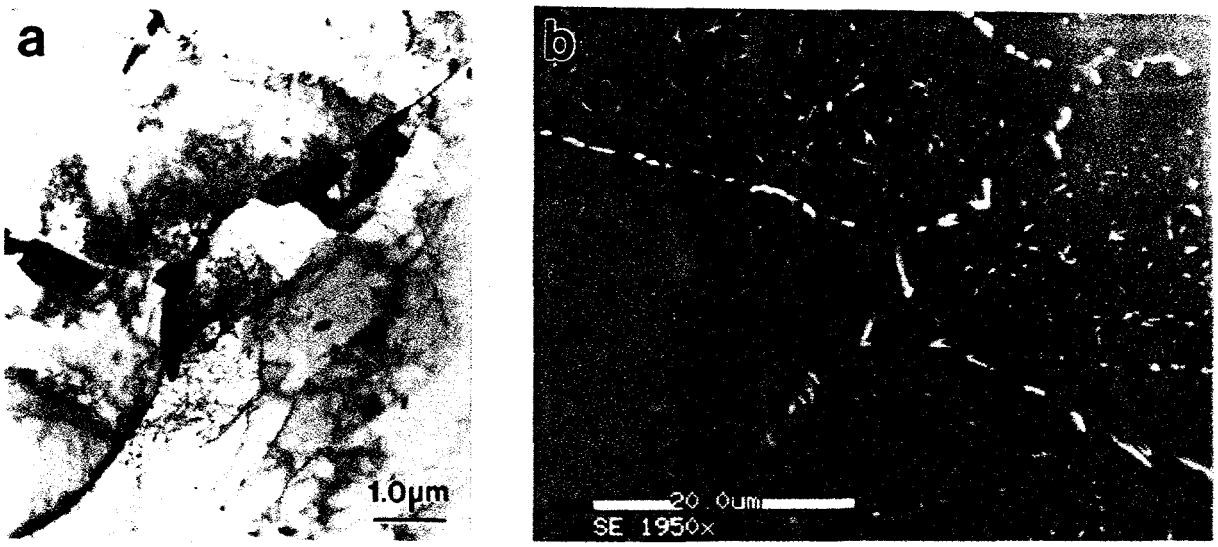

Figure 2: a)Transmission and b) Secondary Electron Micrograghs of the As-Received Material Showing Extent of Intergranular and Intragranular Precipitation

Figure 3: Transmission Electron Micrograghs of the As-Received Material Showing Extensive Deformation Substructure

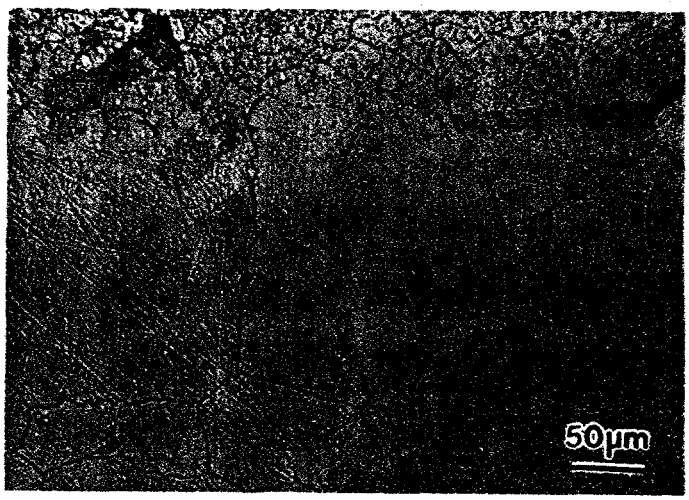

Figure 4: Light Optical Micrograph After an Anneal of 1075°C/24h/Furnace Cool Showing Banding with Duplex Grain Size

Figure 5: Transmission Electron Micrograghs After an Anneal of 1075°C/ 24h/ Furnace Cool Showing No Deformation Substructure and Grain Boundary Carbides

Figure 7a: Transmission Electron Micrograghs After an Anneal of 1075°C/24h/Furnace Cool and Cold Worked Showing High Dislocation Density

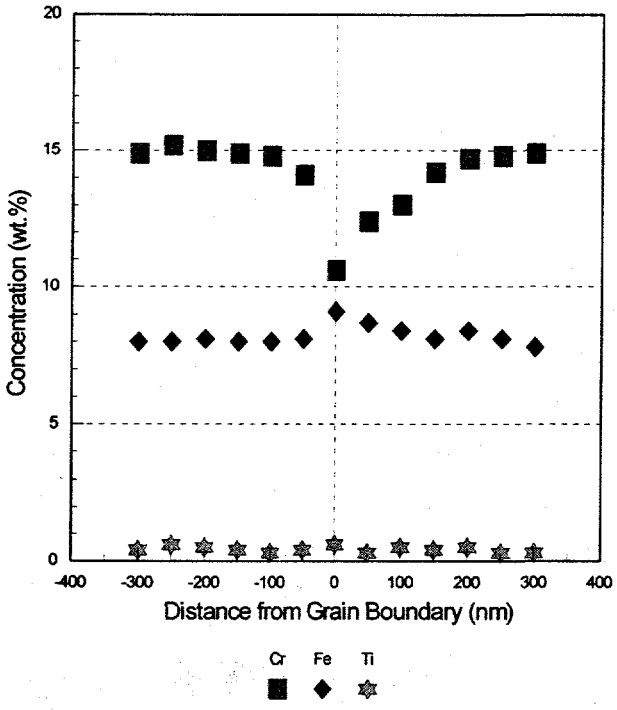

Figure 6: STEM-EDS Cr and Fe Profiles for Grain Boundary after an Anneal of 1075°C/24h/Furnace Cool

Figure 7b: Transmission Electron Micrograghs After an Anneal of 1075°C/24h/Furnace Cool and Cold Worked Showing the Formation of Grain Boundary Voids

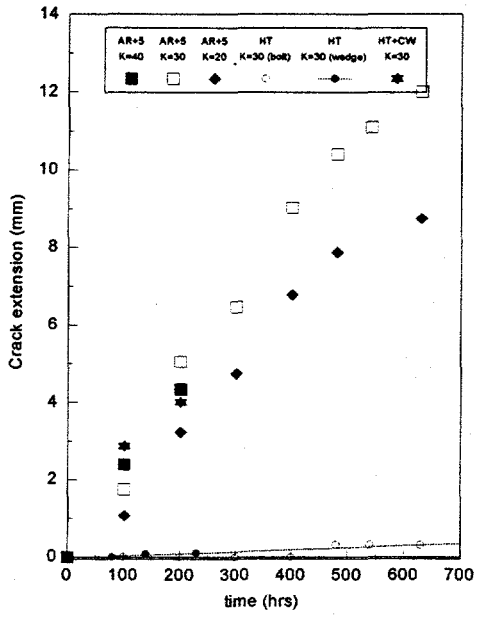

Figure 8: Plot of Crack Length vs. Time for the Three Material Conditions

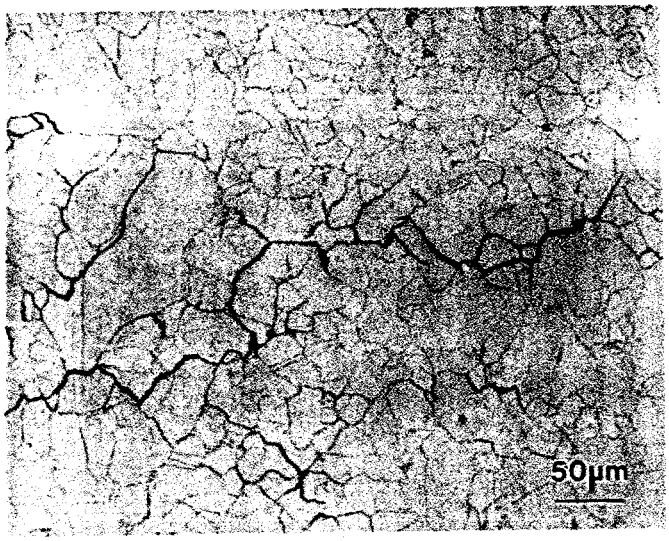

Figure 10: Light Optical Micrographs of the As-Received Material Showing Details of the Primary Intergranular Stress Corrosion Crack

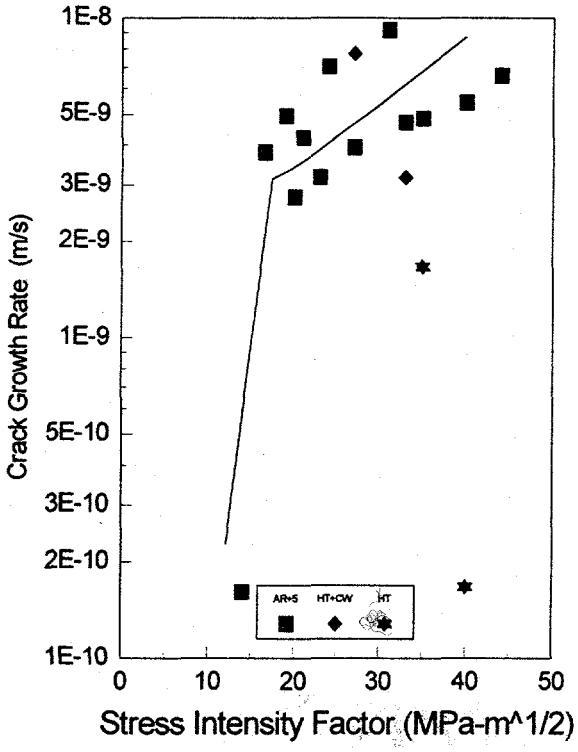

Figure 9: Plot of Crack Growth Rate vs. Stress Intensity Factor for the Three Material Conditions

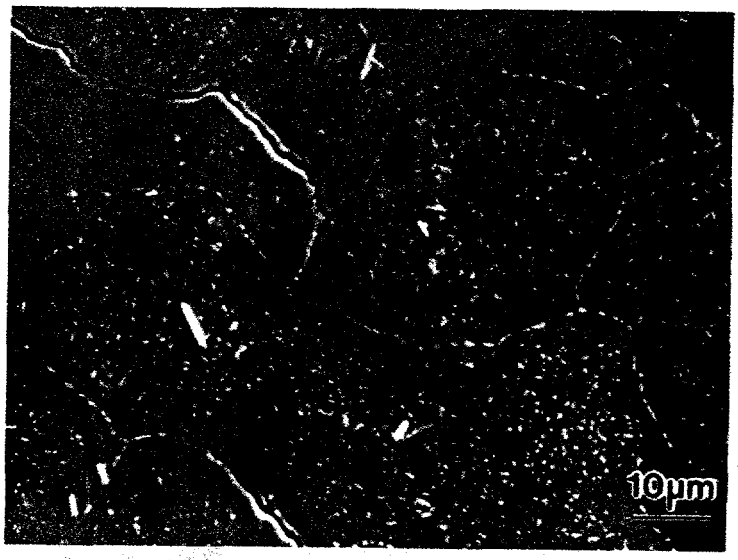

Figure 11a: Secondary Electron Micrographs of the As-Received Material Showing Details of the Primary Intergranular Stress Corrosion Crack

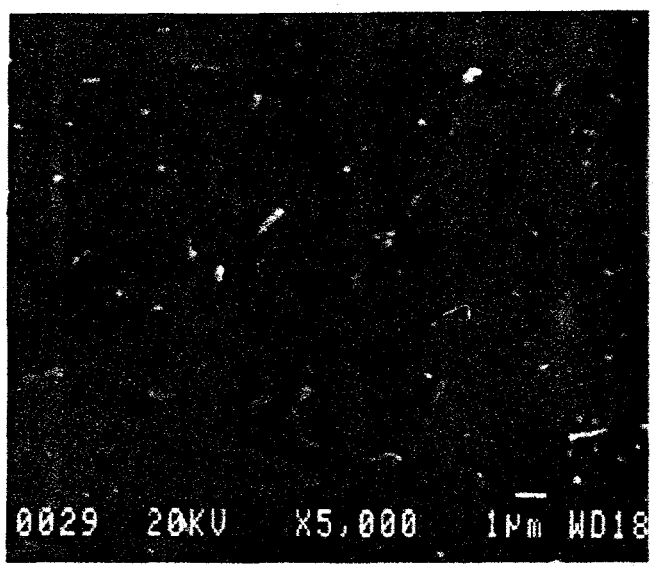

Figure 11b: Secondary Electron Micrographs of the As-Received Material Showing Details of Small Transgranular Crack

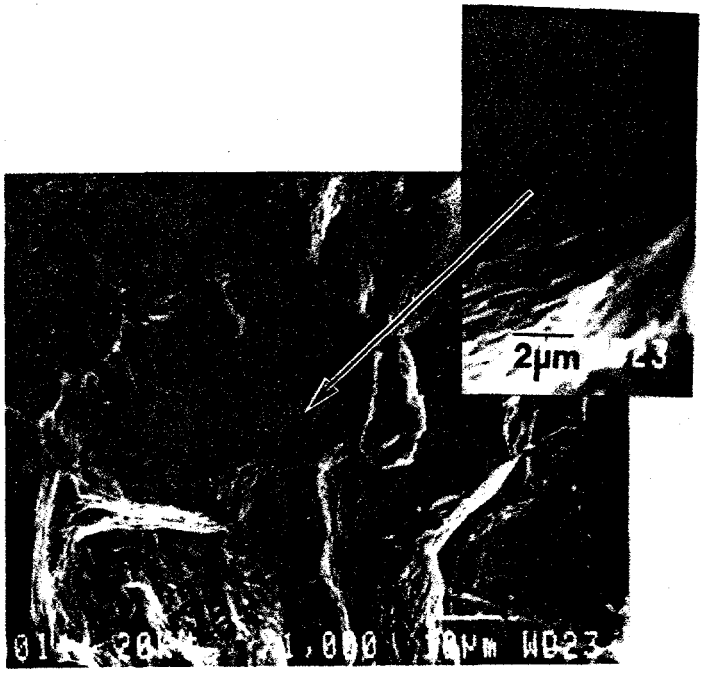

Figure 13: Secondary Electron Fractographs of the As-Received Material Showing The Psuedo-Intergranular Nature of the SCC Fracture Morphology

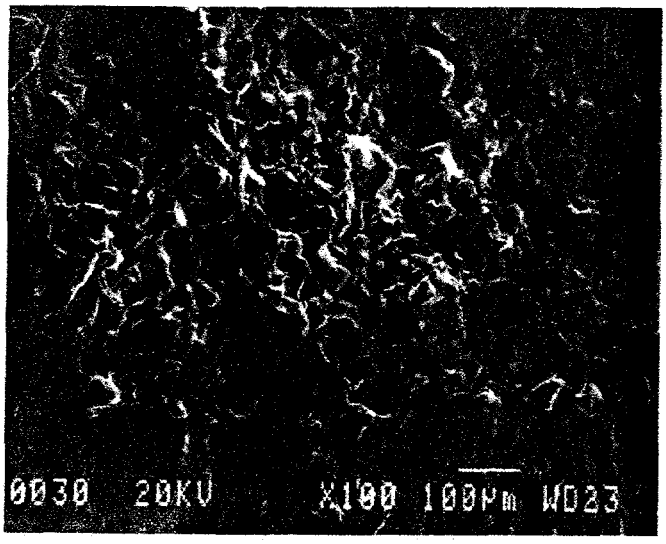

Figure 12: Secondary Electron Fractographs of the As-Received Material Showing The Intergranular Fracture Morphology

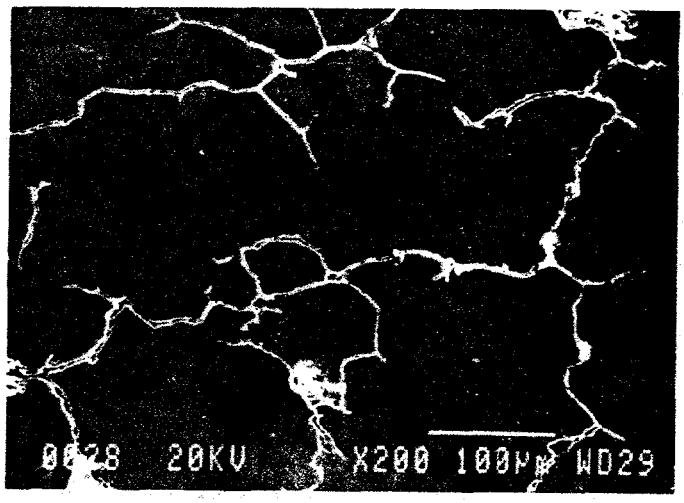

Figure 14: Secondary Electron Micrographs of the 1075°C/24h/Furnace Cool and Cold Worked Material Showing The Intergranular Fracture Morphology

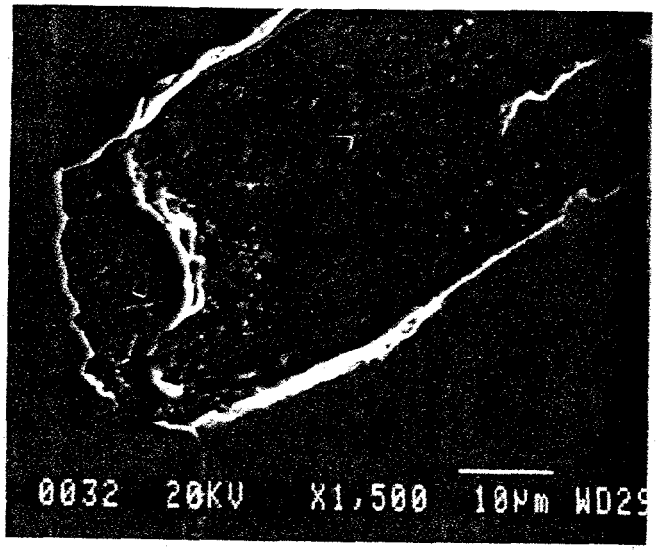

Figure 15: Secondary Electron Micrograph of the 1075°C/24h/Furnace Cool and Cold Worked Material Showing a Grain Boundary Slightly Inclined to the Plane of the Sectioned Sample - Arrow pointing to dendritic carbide

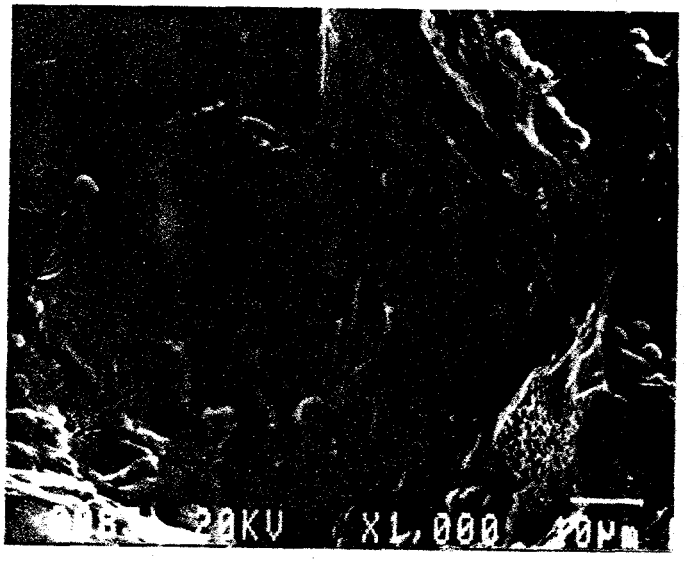

Figure 17: Secondary Electron Fractograph of the 1075°C/24h/Furnace Cool and Cold Worked Material Showing the Relatively Smooth Intergranular Fracture Surfaces

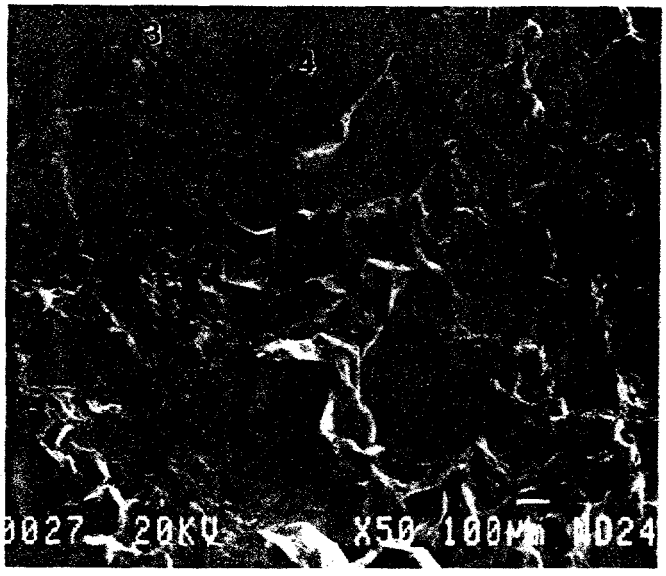

Figure 16: Secondary Electron Fractograph of the 1075°C/24h/Furnace Cool and Cold Worked Material Showing Pronounced Banded Structure - #3 - small grained region and #4 - large grained region

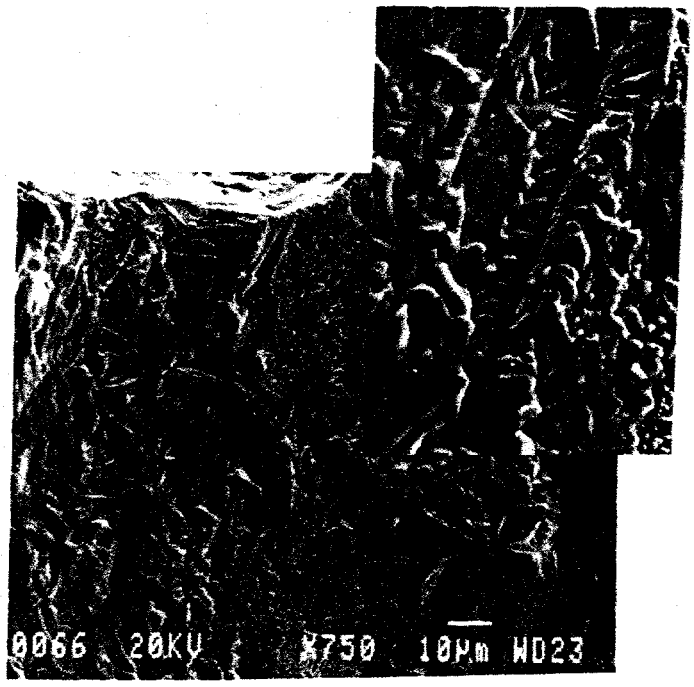

Figure 18: Secondary Electron Fractograph of the 1075°C/24h/Furnace Cool and Cold Worked Material Showing the Rough Intergranular Fracture Surfaces

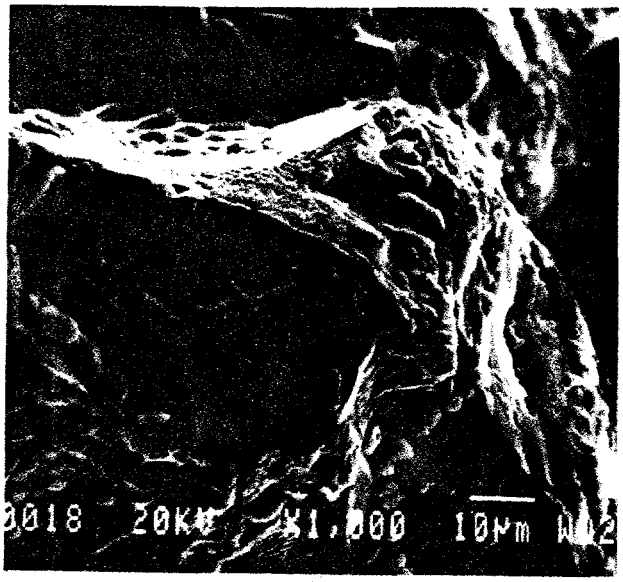

Figure 19: Secondary Electron Fractograph of the 1075°C/24h/Furnace Cool and Cold Worked Material Showing the Mixed Rough and Smooth Intergranular Fracture Surfaces - #1 is on dendritic carbide

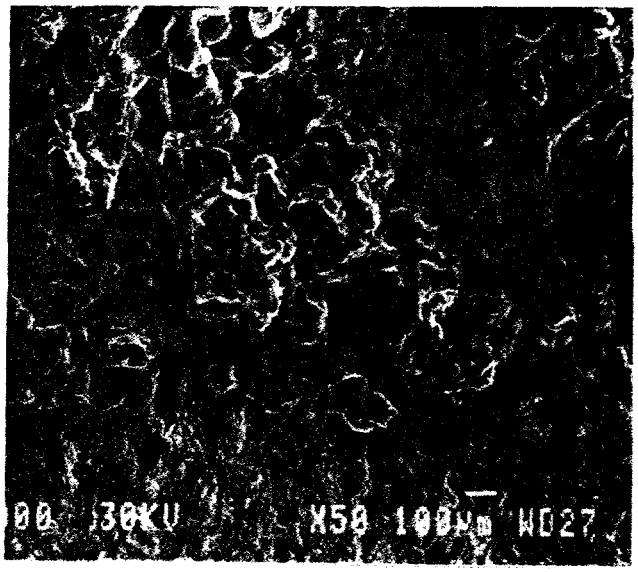

Figure 21: Secondary Electron Fractograph of the 1075°C/24h/Furnace Cool and Cold Worked Material Showing the Intergranular Fracture

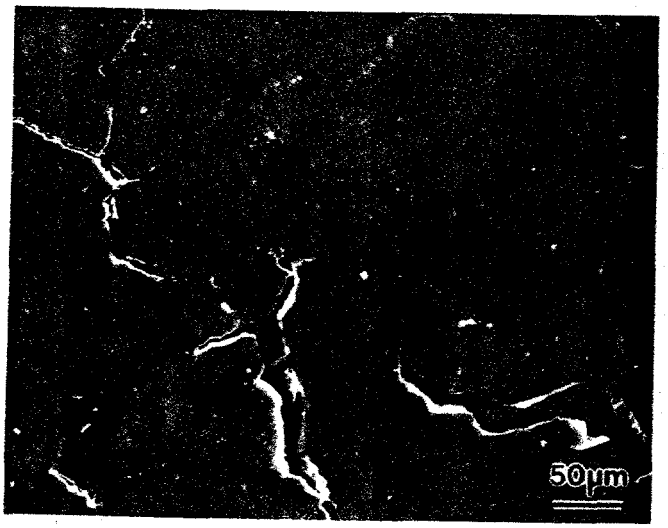

Figure 20: Secondary Electron Micrographs of the 1075°C/24h/Furnace Cool Material Showing The Intergranular Fracture Morphology

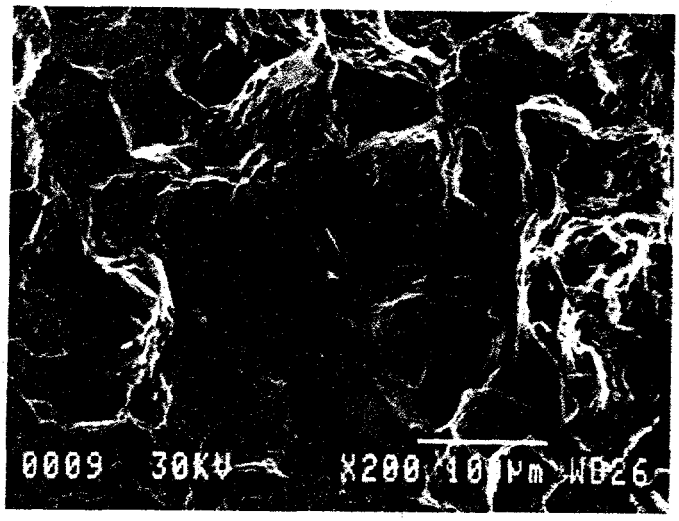

Figure 22: Secondary Electron Fractograph of the 1075°C/24h/Furnace Cool Material Showing the Mixed Rough and Smooth Intergranular Fracture Surfaces